Relating the magnetic coercivity to the L1$_0$ ordered FePd phase in annealed Fe$_x$Pd$_{100-x}$ nanoparticles

Nguyen Hoang Luong[1,2] · Truong Thanh Trung[1] · Tran Thi Hong[1] · Nguyen Hoang Nam[1,2] · Manh-Huong Phan[3] · Péter Jenei[4] · János L. Lábár[4,5] · Jenő Gubicza[4]

Abstract

Rare-earth-free or iron-based permanent nanomagnets are emerging as promising candidates for energy-conversion and information technologies. In this interest, Fe$_x$Pd$_{100-x}$ nanoparticles ($x = 50$, 55, 60, and 63) were prepared from iron acetate and palladium acetate by sonoelectrodeposition. After annealing the nanoparticles at various temperatures from 450 to 700 °C for 1 h, structural changes were observed, and the samples exhibit hard magnetic properties that depend strongly on chemical composition and annealing temperature. The major phase in the as-prepared nanoparticles has a disordered face-centered cubic structure, which, upon annealing, transforms into a multi-phase material containing a L1$_0$ ordered FePd phase. The fractions of different phases present in the annealed samples, including that of the L1$_0$ phase as functions of chemical composition and annealing temperature, are quantified by means of X-ray diffraction and scanning transmission electron microscopy. Magnetic measurements show the desirable hard magnetic properties for the samples annealed at 550–600 °C. A correlation between the magnetic coercivity and the L1$_0$ ordered FePd phase fraction is established for the first time in the Fe$_x$Pd$_{100-x}$ nanoparticles.

Keywords FePd · Sonoelectrodeposition · Magnetic nanoparticles · Hard magnetic materials · L1$_0$ phase

1 Introduction

In recent years, the synthesis of magnetic nanostructures has been investigated for various applications due to their unique structural, electrical, and magnetic properties [1–5]. FePt, CoPt, and FePd nanoparticles have attracted considerable attention for their potential use in magnetic applications, including ultrahigh-density magnetic recording media and high-performance permanent magnets, due to the high magnetocrystalline anisotropy of their L1$_0$-type ordered structure [6–14]. The ordered face-centered tetragonal (fct) L1$_0$ FePd alloy is magnetically hard and exhibits a magnetocrystalline anisotropy energy density, K_u, of 1.8×10^7 erg/cm^3 [6, 15]. This value of K_u is lower than $6.6–10 \times 10^7$ erg/cm^3 for FePt and 4.9×10^7 erg/cm^3 for CoPt [6]. To be able to write information onto media, high K$_u$ recording materials usually require high writing fields. Owing to its high magnetocrystalline anisotropy, FePt media require a much higher writing field than those currently applicable from magnetic recording heads [16]. Therefore, L1$_0$ FePd may be more preferable than its L1$_0$ counterparts for application in magnetic recording media [16–19]. As for FePt and CoPt materials, the as-prepared FePd nanoparticles are in the disordered face-centered cubic (fcc) phase. Appropriate annealing is needed to transform the disordered fcc phase into an ordered fct L1$_0$ phase.

Several approaches have been employed to prepare FePd nanoparticles, including epitaxial growth by electron beam

✉ Nguyen Hoang Luong
  luongnh@hus.edu.vn

✉ Jenő Gubicza
  jeno.gubicza@ttk.elte.hu

1 University of Science, Vietnam National University, Hanoi, 334 Nguyen Trai, Hanoi, Vietnam

2 Nanotechnology Program, Vietnam Japan University, Vietnam National University, Hanoi, Luu Huu Phuoc, Hanoi, Vietnam

3 Department of Physics, University of South Florida, Tampa, FL 33620, USA

4 Department of Materials Physics, Eötvös Loránd University, Pázmány Péter sétány 1/A, 1117 Budapest, Hungary

5 Institute for Technical Physics and Materials Science, Centre for Energy Research, Budapest, Hungary

deposition [16, 20–23], chemical synthesis [24–27], modified polyol process [28–30], microwave irradiation [31], and one-pot pyrolysis method [32]. In 2020, Shao et al. [33] introduced a eutectic crystallization approach into the synthesis of hard magnetic FePd nanoparticles. FePd films have also been prepared using sputtering [19, 34–39], thermal evaporation [40], molecular beam epitaxy [35, 41], and electrodeposition [42–44]. We previously reported on the magnetic properties of FePd nanoparticles prepared by sonochemistry [45]. Very recently, we have used the sonoelectrodeposition method for the preparation of FePd nanoparticles with tunable chemical compositions [46, 47]. Sonoelectrodeposition is a technique combining the advantages of sonochemistry and electrodeposition [48]. Some of the beneficial effects of sonoelectrodeposition include acceleration of mass transport, cleaning and degassing of the electrode surface, and an increased reaction rate [49].

It is known that annealing FePd nanoparticles transforms the fcc phase into a multi-phase material containing disordered and $L1_0$ ordered phases [47]. Due to the presence of the $L1_0$ ordered phase with high magnetocrystalline anisotropy, it is essential to examine relationship between the magnetic coercivity and the $L1_0$ ordered FePd phase fraction in the FePd nanoparticles. While a strong correlation between the magnetic coercivity, H_C, and the $L1_0$ ordered phase fraction, f_o, (also its chemical order, s_0) has been established for FePt and CoPt thin films due to the strong dependence of magnetocrystalline anisotropy on f_o [50–52], to the best of our knowledge, no report has dealt with this relationship in FePd nanoparticle systems. In a previous work [45], we observed some dependence of the coercivity on the degree of the chemical order in Fe_xPd_{100-x} nanoparticles but could not quantify the volume fractions of the disordered and ordered phases that coexisted in these nanoparticles, due to the lack of a thorough structural analysis. As for $Fe_{60}Pd_{40}$ and $Fe_{55}Pd_{45}$ nanoparticles synthesized by sonoelectrodeposition, we also observed a strong annealing temperature dependence of the structural and magnetic properties; however, their correlations were not established [46, 47]. This arose from the fact that volume fractions of disordered and $L1_0$ ordered FePd phases, which, as mentioned above, usually coexisted in the FePd nanomaterials, were not quantified in the previous studies [27–30, 45, 46]. An in-depth structural analysis can be performed by the combination of advanced characterization techniques such as X-ray diffraction (XRD), transmission electron microscopy (TEM), scanning TEM (STEM) and energy-dispersive spectroscopy mapping in TEM (TEM-EDS).
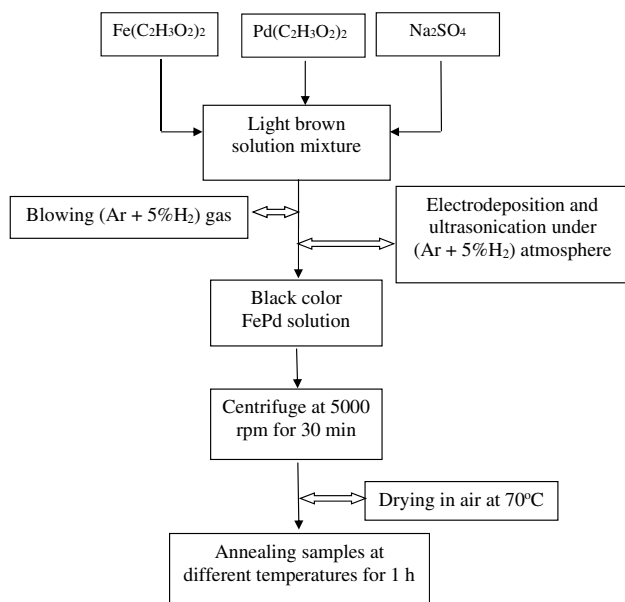
To establish the relationship between the coercivity and the $L1_0$ ordered phase fraction in FePd nanoparticles, we have synthesized and characterized Fe_xPd_{100-x} ($x = 50$, 55, 60, and 63) nanoparticles prepared by sonoelectrodeposition and annealed at different temperatures (450–700 °C).

The volume fractions of different phases present in these samples, including that of the $L1_0$ ordered phase as functions of chemical composition and annealing temperature, are quantified using a combination of XRD with TEM and STEM techniques. The analyzed results show evidence that annealing promoted the growth of the $L1_0$ ordered phase but also created other phases, whose volume fractions also varied depending upon the chemical composition. The highest fraction of the $L1_0$ ordered phase was observed at annealing temperatures of 550–600 °C, irrespective of the Fe/Pd ratio in the samples. Optimal hard magnetic properties are also achieved at these annealing temperatures. These comprehensive analyses, performed on Fe_xPd_{100-x} nanoparticles with a wide range of doping concentrations, have allowed us to establish for the first time, a correlation between the coercivity and the $L1_0$ ordered phase fraction in FePd nanosystems.

2 Experimental

The synthesis of Fe_xPd_{100-x} nanoparticles was conducted by sonoelectrodeposition as described in [47]. The volume of the electrolysis cell was 100 ml containing iron(II) acetate [$Fe(C_2H_3O_2)_2$], palladium(II) acetate [$Pd(C_2H_3O_2)_2$], and Na_2SO_4, which were mixed under (Ar + 5%H_2) atmosphere. Different Fe/Pd ratios were achieved by changing the ratio of iron acetate to palladium acetate. After deposition, FePd nanoparticles were washed and separated from the solution by adding ethanol and centrifuging (Hettich Universal 320) at 5000 rpm for 30 min. The as-received powders were dried in air at 70 °C for 30 min. The chemical composition of the FePd nanoparticles was studied using energy-dispersive spectroscopy (EDS OXFORD-ISIS 300). The EDS measurements revealed that the chemical compositions of the four Fe_xPd_{100-x} samples investigated in this study were $x = 50$, 55, 60 and 63. The as-prepared samples were then annealed at different temperatures $T_{an} = 450$, 500, 550, 600, 650, and 700 °C for 1 h under continuous flow of Ar + 5%H_2 gas mixture. In this process, first the samples were heated up to a desired temperature T_{an} at a heating rate of 5 °C/min. Then, the powders were kept at the selected temperature T_{an} for 1 h and finally furnace cooled to room temperature. A schematic diagram of the preparation process is illustrated in Fig. 1.

The size and the morphology of the powder particles were studied by TEM. First, the investigated powder was dissolved in distilled water and dropped on a thin carbon film stretched over a Cu-grid. TEM and STEM measurements were carried out in a Titan Themis G2 200 TEM operated at 200 keV. TEM images were recorded with a FEI CETA 16 M camera, while STEM images were collected with a Fishione HAADF detector. EDS elemental maps were taken with a FEI Super-X EDX System using Velox software. The phase composition of the as-prepared and annealed samples was studied by XRD using a

Philips Xpert powder diffractometer with CuKα radiation (the wavelength was 0.15418 nm) and Bragg–Brentano geometry. The large fluorescence radiation of the iron containing phases caused by the CuKα X-rays was eliminated using a pyrolitic graphite secondary monochromator. The average crystallite size for each phase was determined from the broadening of the first XRD peak using the Scherrer formula [53]. The phase fraction of the different phases was determined as the fraction of the integrated intensity of the studied phase in the whole diffractogram. The intensity was calculated as the area under the XRD peaks after background subtraction applying the following steps. First, the area under each XRD peak after background subtraction was determined. For strongly overlapping peaks, Lorentzian functions were used to fit these reflections and the areas under the fitted profiles were used for the determination of the integrated intensity. Then, the sum of the integrated intensities (areas under the peaks) of the available reflections was calculated for each phase. Finally, the fraction of a selected phase was characterized with the fraction of its intensity in the total XRD pattern. The magnetic properties of the samples were characterized at room temperature using a Vibrating Sample Magnetometer (VSM).

3 Results and discussion

## 3.1 Phase composition of the as-prepared and annealed nanoparticles

The phase compositions of the as-prepared and annealed Fe$_x$Pd$_{100-x}$ powders were analyzed by XRD and are listed in Table 1. As an example, the XRD patterns of as-prepared and annealed (at 600 and 700 °C) Fe$_{60}$Pd$_{40}$ samples are shown in Fig. 2. It can be seen in Table 1 that irrespective of the Fe/Pd ratio in the samples, the main phase in the as-prepared state is a fcc phase with a lattice constant of 0.3897 ± 0.0006 nm, which is close to the lattice parameter of pure Pd (0.3891 nm, PDF: 00–0,050,681). This observation suggests that this fcc phase contains mainly Pd. On the other hand, the atomic size of Fe is only 4% smaller than that of Pd, therefore substitutional iron alloying in this phase cannot be excluded. In our study, this phase is denoted as a disordered Pd(Fe). The intensity fraction of this phase is 80–90% and the crystallite size is about 10 nm as determined by XRD, irrespective of the chemical composition of the as-prepared powder. The secondary phase peaks are very broad and weak (see Fig. 2a), and the phase identification according to these reflections was unsuccessful. These broad peaks may be fingerprints of an amorphous phase as suggested by the TEM selected area electron diffraction (SAED) results, which are presented and discussed below. Most probably, this phase contains the majority of Fe in the as-prepared powders. Probably, the iron is oxidized and may be present in e.g., oxide-hydroxide (amorphous) compounds. It should be noted that different X-ray absorption of the various phases can alter the values of their XRD intensity fractions. Namely, higher absorption reduces the measured intensity fraction and additionally makes the identification of the weak peaks difficult [54]. In the present case, a large absorption can be caused by high X-ray fluorescence of iron atoms irradiated by CuKα radiation. For a reliable quantitative XRD phase analysis, the Brindley absorption criterion must be fulfilled, i.e., the value of μD should be less than 0.01, where μ is the absorption coefficient and D is the particle size [55]. The absorption coefficient of both Fe and Pd—which are the main constituents of the presently studied materials—is about 2300 cm^{-1}, therefore the effect of absorption on the X-ray intensity scattered by the different Fe and Pd containing phases is similar. Thus, the XRD intensity ratio can be used for the quantification of the phase fractions in our study. In addition, the crystallite size varies between 20 and 50 nm for most phases of the studied materials according to XRD, therefore, the value of μD is between 0.005 and 0.012, i.e., the Brindley criterion of the reliable quantitative analysis is fulfilled.

Table 1 The phase composition and the crystallite sizes of the different phases determined by XRD for the as-prepared Fe_xPd_{100-x} ($x = 50, 55, 60,$ and 63) nanoparticles and the specimens annealed at 450, 500, 550, 600, 650, and 700 °C for 1 h

Ann. Temp [°C]	Phase	Intensity fraction (%)				Crystallite size (nm)			
		$Fe_{50}Pd_{50}$	$Fe_{55}Pd_{45}$	$Fe_{60}Pd_{40}$	$Fe_{63}Pd_{37}$	$Fe_{50}Pd_{50}$	$Fe_{55}Pd_{45}$	$Fe_{60}Pd_{40}$	$Fe_{63}Pd_{37}$
As-prepared	fcc Pd(Fe)	94	90	88	77	9	8	9	10
	Unknown phase	6	10	12	23				
450	fcc Pd(Fe)	71	81	62	45	24	21	29	23
	bcc Fe	20	18	21	25	57	50	70	48
	Fe_3O_4	9	–	–	22	29	–	–	30
	$L1_0$ FePd	–	–	17	5	–	–	37	–
	Unknown fcc phase	–	1	–	2	–	–	–	37
500	fcc Pd(Fe)	61	47	57	37	20	26	22	25
	bcc Fe	2	8	3	30	71	41	58	57
	Fe_3O_4	2	1	6	5	32	28	30	20
	$L1_0$ FePd	35	41	34	25	22	26	27	27
	Unknown fcc phase		4		2		28		28
550	fcc Pd(Fe)	60	41	34	46	21	20	31	20
	bcc Fe	2	8	4	10	49	43	47	50
	Fe_3O_4	1	–	–	–	–	–	–	–
	$L1_0$ FePd	37	39	62	41	46	42	37	44
	Unknown fcc phase	–	12	–	2	–	43	–	21
600	fcc Pd(Fe)	50	18	43	36	24	28	18	23
	bcc Fe	2	7	2	35	53	51	49	57
	$L1_0$ FePd	48	71	55	29	41	31	29	51
	Unknown fcc phase	–	4	–	–	–	36	–	–
650	fcc Pd(Fe)	53	–	–	36	26	–	–	18
	fcc γ-FePd	19	80	76	46	74	53	49	34
	bcc Fe	1	2	11	4	46	67	58	66
	$L1_0$ FePd	27	18	13	14	47	22	24	35
700	fcc Pd(Fe)	62	–	–	30	26	–	–	20
	fcc γ-FePd	16	90	81	42	44	60	43	51
	bcc Fe	–	1	7	3	–	59	49	38
	$L1_0$ FePd	22	9	12	25	42	42	28	31

Figure 3a shows a typical TEM bright-field (BF) image on a particle cluster in the as-prepared $Fe_{60}Pd_{40}$. The contrast differences in the STEM high-angle annular dark-field (HAADF) image (see Fig. 3b) suggest chemical heterogeneities in the different particles of the agglomerate. Indeed, the Fe and Pd elemental maps in Fig. 3c and d, respectively, indicate that there is an abundance of Pd in the particles exhibiting bright contrast. Most probably, these particles are related to the Pd-rich fcc phase observed by XRD (see Fig. 2a). The SAED pattern in Fig. 3e shows spots which correspond to Pd reflections as revealed by the diffractogram obtained by integrating the intensity in the SAED pattern (see Fig. 2f). The broad continuous rings may be related to an amorphous phase, which must contain the majority of Fe since the sharp spots in the SAED pattern correspond to the fcc Pd peaks. EDS suggests that the latter phase contains iron, therefore, it is denoted as Pd(Fe).

Annealing the powders at 450 °C resulted in the formation of a significant amount of body-centered cubic (bcc) iron phase (see Table 1). Most probably, this phase was obtained by the crystallization of the assumed amorphous iron oxide-hydroxide compounds in the as-prepared sample. In addition, an ordered $L1_0$ FePd phase (PDF: 00–002-1440) started to develop for the $Fe_{60}Pd_{40}$ and $Fe_{63}Pd_{37}$ samples. This phase became significant and has intensity fractions between 25 and 41% for all of the four compositions at 500 °C. The volume fraction of the $L1_0$ ordered FePd phase increased with increasing the annealing temperature, and this phase became dominant at 600 °C, as shown in Fig. 2b. As an example, Fig. 4a shows $L1_0$ FePd particles in the $Fe_{60}Pd_{40}$ sample annealed at 550 °C as suggested by TEM-EDS performed on the area, denoted by the rectangle in the HAADF image in Fig. 4b. Chemical analysis indicated that the composition is $Fe_{50}Pd_{50}$ in the investigated area.
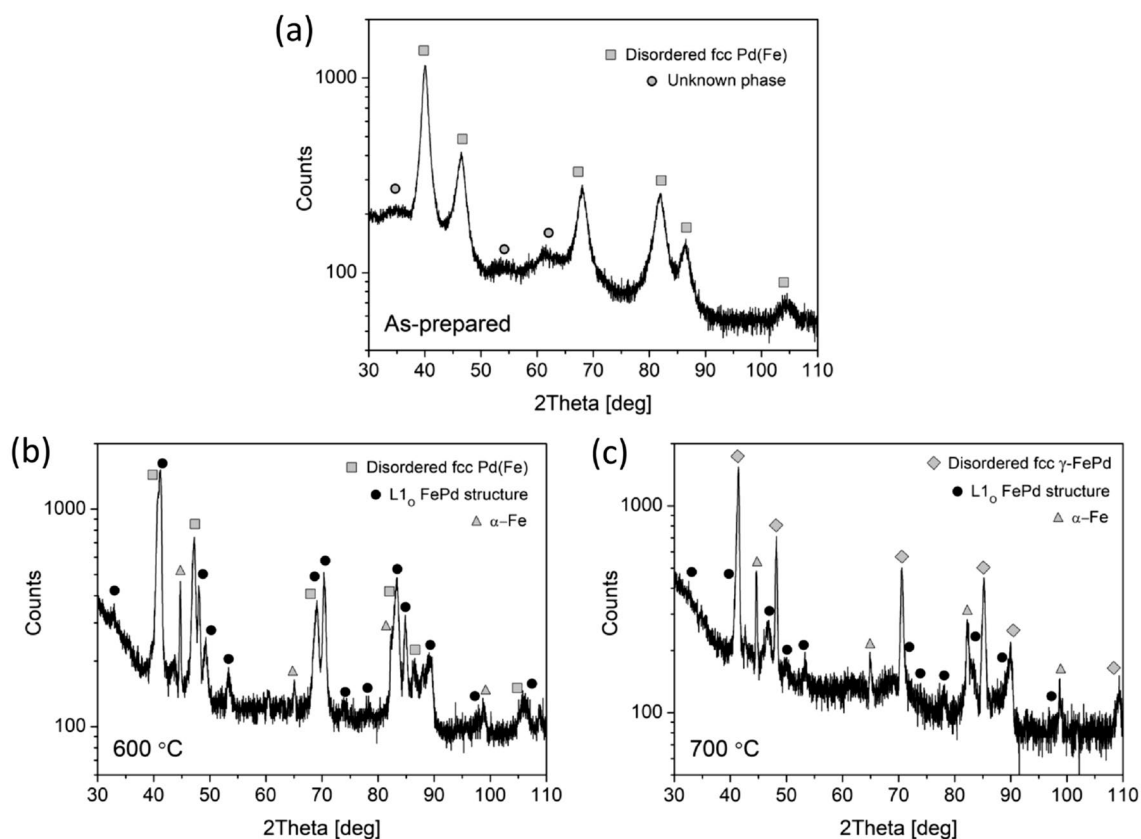
**Fig. 2** X-ray diffractograms measured on the **a** as-prepared and **b**, **c** annealed $Fe_{60}Pd_{40}$ nanoparticles. The intensity is in logarithmic scale

The element distribution is relatively homogeneous in the whole particle cluster as shown in Fig. 4c, d. In this sample, particles with Pd- and Fe-rich compositions are shown in Fig. 5. The large grain in the center and the small grain at the top-right corner of the image (the latter is indicated by a yellow arrow) are enriched in Fe and Pd, respectively. Thus, it seems that different crystalline phases are present in different particles in the powder. In addition, the sizes of the particles are in accordance with the crystallite sizes determined by XRD (about 20–50 nm as shown in Table 1).

Further increase of the annealing temperature above 550 °C yielded a reduction in the fraction of the L1₀ ordered FePd phase (see Table 1). Instead, a fcc γ-FePd phase (or disordered A1 phase as denoted in [56]) became the major phase at 650–700 °C as illustrated in Fig. 2c. At these temperatures, there was an effect of the chemical composition on the intensity fractions of the crystalline phases. Namely, for $Fe_{55}Pd_{45}$ and $Fe_{60}Pd_{40}$, there was an abundance of the fcc γ-FePd phase (the intensity fraction is 80–90%), while for $Fe_{50}Pd_{50}$ and $Fe_{63}Pd_{37}$, a significant fraction of fcc Pd(Fe) remained in the samples even after annealing at 700 °C for 1 h (see Table 1). This difference is illustrated in the comparison of XRD patterns obtained for the samples $Fe_{50}Pd_{50}$ and $Fe_{55}Pd_{45}$ annealed at 700 °C in Fig. 6.

3.2 Magnetic properties

To understand the effects of chemical composition and annealing on the magnetic properties of Fe_xPd_{100-x} nanoparticles, magnetic hysteresis *M(H)* loops were taken at room temperature for all the samples utilizing a VSM. Figure 7 shows room-temperature *M(H)* curves of the $Fe_{50}Pd_{50}$ (x = 50) nanoparticles annealed at various temperatures. It is obvious that these nanoparticles show a hard magnetic characteristic at room temperature. A similar trend has been observed for Fe_xPd_{100-x} samples with x = 55, 60, and 63. For x = 50, the coercive field (H_C) of the sample annealed at 450 °C was about 0.26 kOe. The H_C increased with increasing annealing temperature and reached a maximum value of 1.08 kOe at 550 °C. With further increase of the annealing temperature, H_C decreased and had a low value of about 0.38 kOe at 700 °C. Annealing-temperature dependences of H_C for Fe_xPd_{100-x} (x = 50, 55, 60 and 63) are shown in Fig. 8a. As can be seen from this figure, the samples with different x values show a similar annealing temperature-dependent coercivity trend. The coercivity of the nanoparticles increases with increasing annealing temperature, achieves a maximum value at 550–600 °C, and then decreases for higher annealing temperatures (e.g., 700 °C).
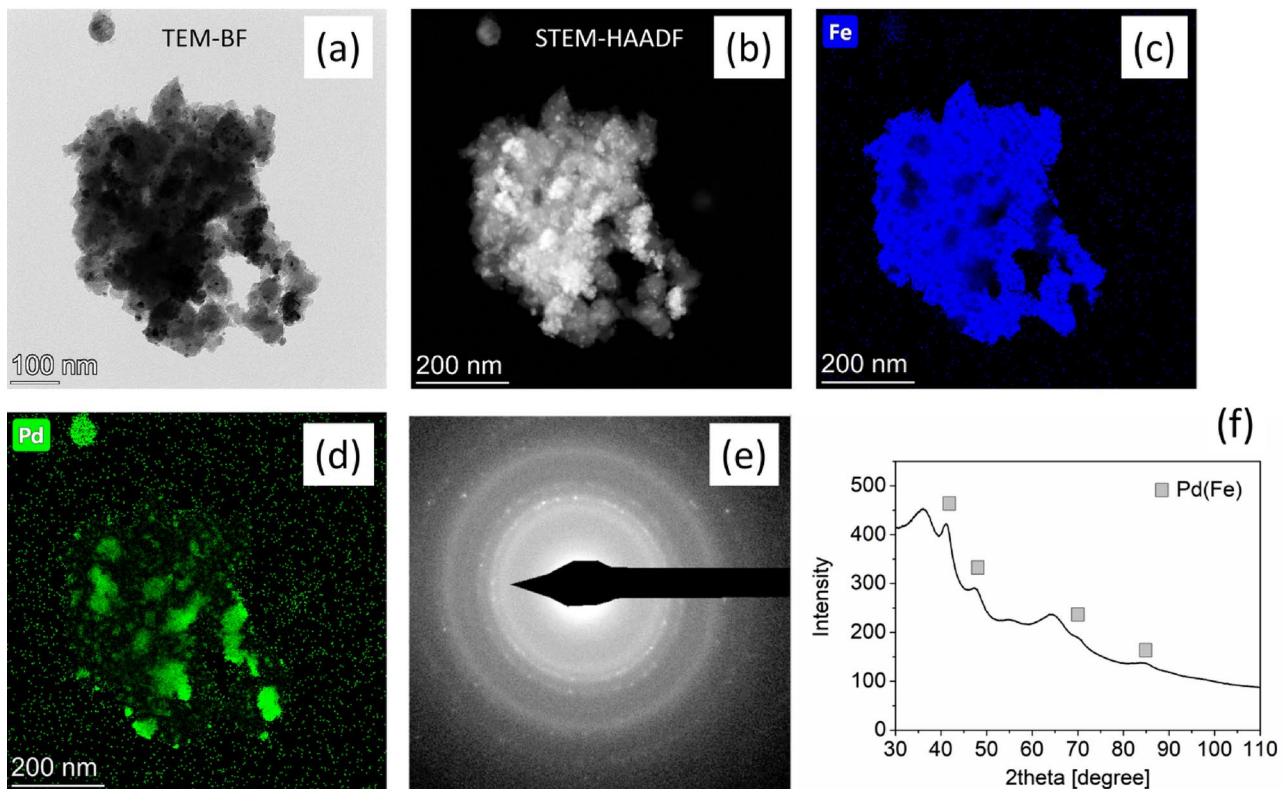
Fig. 3 A powder particle cluster in the as-prepared $Fe_{60}Pd_{40}$ as revealed by TEM. **a** TEM-BF image, **b** STEM-HAADF image, **c** Fe elemental map taken by EDS, **d** Pd elemental map obtained by EDS, **e** SAED pattern taken on the particle cluster. The diffractogram in **f** was obtained by integrating the intensity along concentric rings in the SAED in **e** and the reciprocal space variable was converted to Bragg angle using the same wavelength as applied in the XRD experiments (0.15418 nm) to obtain a pattern comparable with the XRD results

A similar trend was observed for the coercivity of Fe_xPd_{100-x} nanoparticles prepared by sonochemistry in our previous study [45]. It should be noted, however, that the coercivity values obtained in [45] and in this study are different for the same composition and annealing temperature. This is most likely due to the different synthesis techniques used in [45] (sonochemistry) and in this study (sonoelectrodeposition). Sonochemistry is the method in which molecules undergo a chemical reaction due to the application of powerful ultrasound radiation [57, 58]. This method is based on the cavitation phenomenon, which is the formation, growth, and implosive collapse of bubbles in a liquid medium [59, 60]. Ultrasonic cavitation leads to a significant change in morphology without affecting chemical composition [61], thus affecting the coercivity value of the nanomaterials. As stated above in the Introduction section, sonoelectrodeposition is a technique that combines the advantages of both sonochemistry and electrodeposition. In the sonoelectrodeposition, a current is applied, and the current density may affect the coercivity value of the sample. An example of the influence of the current density on the coercivity value can be found in [62] for CoPt nanoparticles. In this work, among Fe_xPd_{100-x} samples investigated,

the $x = 60$ composition shows the highest H_C of 2.07 kOe. The decrease of H_C at high temperatures (650, 700 °C) can be attributed to the reduction of the volume fraction of the ordered FePd phase (Table 1), as well as the decrease of the degree of atomic ordering in these nanoparticles [50–52]. The maximum value of H_C observed in this work is comparable to the values obtained by other groups [7, 25, 28, 29, 33]. Watanabe et al. [28] used the modified polyol process to synthesize $Fe_{49.2}Pd_{50.8}$ nanoparticles. The authors showed that a H_C value of 2.04 kOe at 5 K was obtained for the sample annealed at 600 °C for 1 h. We note that the $Fe_{49.2}Pd_{50.8}$ nanoparticles studied in [28] were annealed only at one temperature of 600 °C and no value of coercivity at room temperature was reported. Gajbhiye et al. [29] also used the modified polyol process to prepare $Fe_{43}Pd_{57}$ nanoparticles and annealed the samples at 450, 550 and 600 °C for 1 h. They reported H_C values of 1.18 kOe and 1.3 kOe at 300 K for $Fe_{43}Pd_{57}$ samples annealed at 550 and 600 °C, respectively. According to Gajbhiye et al. [29], the enhanced coercivity of the sample annealed at 600 °C compared to that annealed at 550 °C is due to a better atomic ordering in the $L1_0$ phase. However, the annealing at 600 °C was noticed to cause severe agglomeration of FePd nanoparticles, which

Fig. 4 A powder particle cluster in the Fe$_{60}$Pd$_{40}$ sample annealed at 550 °C. **a** TEM-BF image, **b** STEM-HAADF image, **c** Fe elemental map taken by EDS, **d** Pd elemental map obtained by EDS
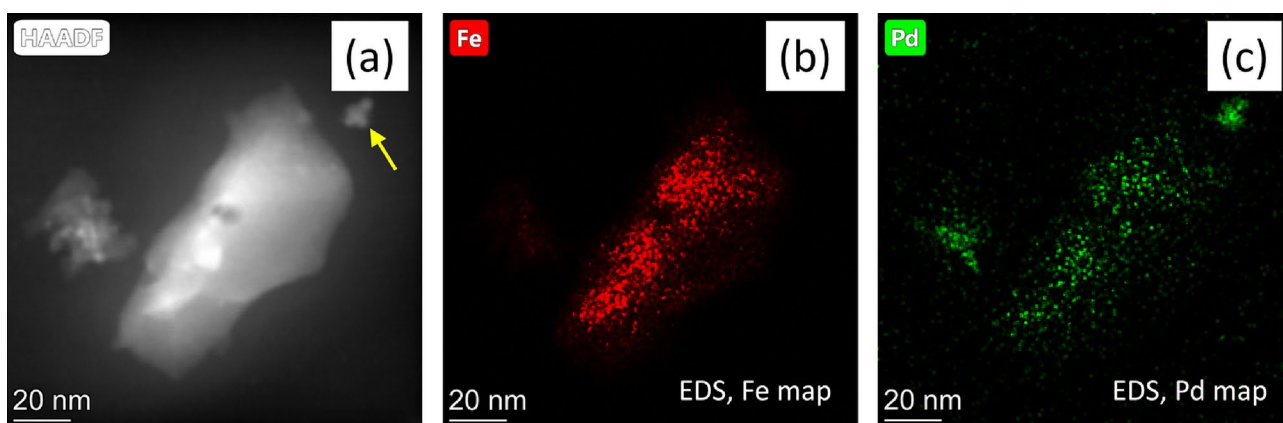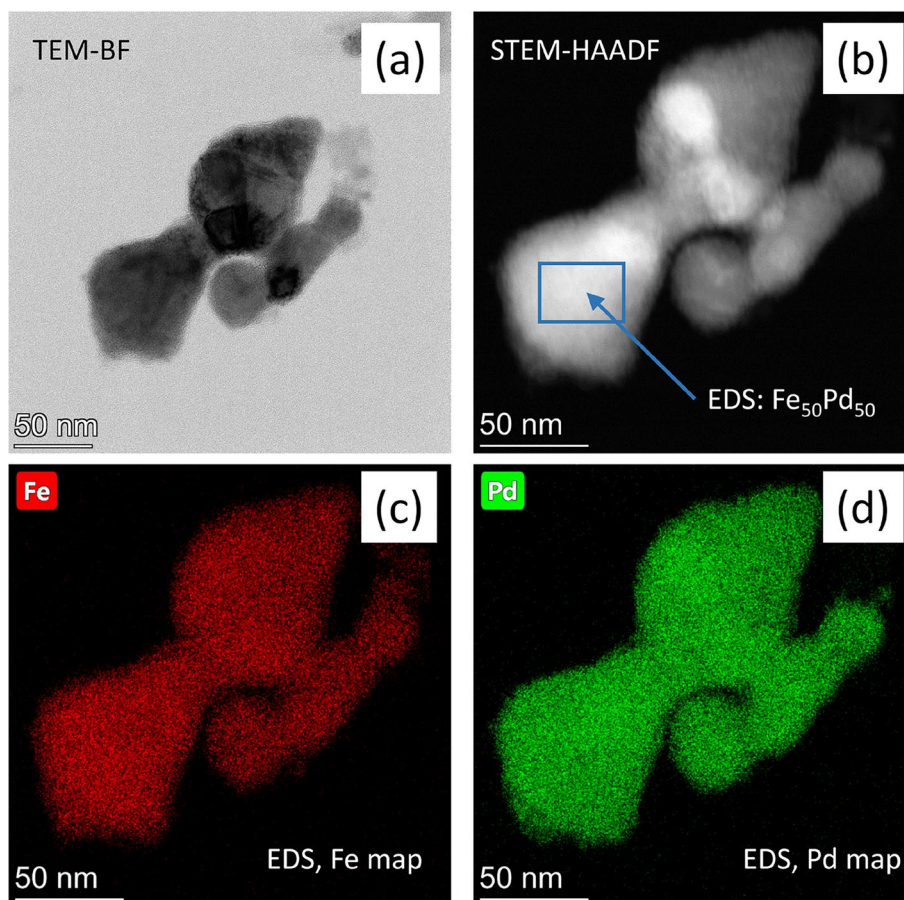

Fig. 5 Powder particles with different compositions in the Fe$_{60}$Pd$_{40}$ sample annealed at 550 °C. **a** STEM-HAADF image, **b** Fe elemental map taken by EDS, **c** Pd elemental map obtained by EDS. The yellow arrow at the top-right corner of the HAADF image indicates a Pd-rich particle

is detrimental for technical applications. Hou et al. [25] prepared Fe$_{48}$Pd$_{52}$ nanoparticles by a chemical method and annealed them at 550, 600, and 700 °C for 30 min. They observed that the room-temperature coercivity of the samples increased with increasing annealing temperature, and it reached a maximum H_C value of ~ 2 kOe for the samples annealed at 600 °C. Further increase of the annealing

temperature was reported to decrease the coercivity, suggesting the formation of a new soft phase, Fe$_3$Pd, at higher temperatures. In the eutectic crystallization approach introduced by Shao et al. [33], the authors applied the eutectic salt melt route, namely, a powder metallurgical method, which uses KCl-LiCl as a salt solvent to prepare FePd nanoparticles. This is a one-pot synthesis of hard magnetic FePd
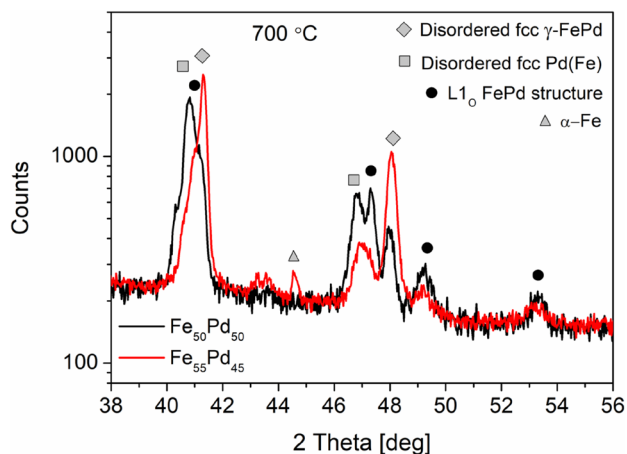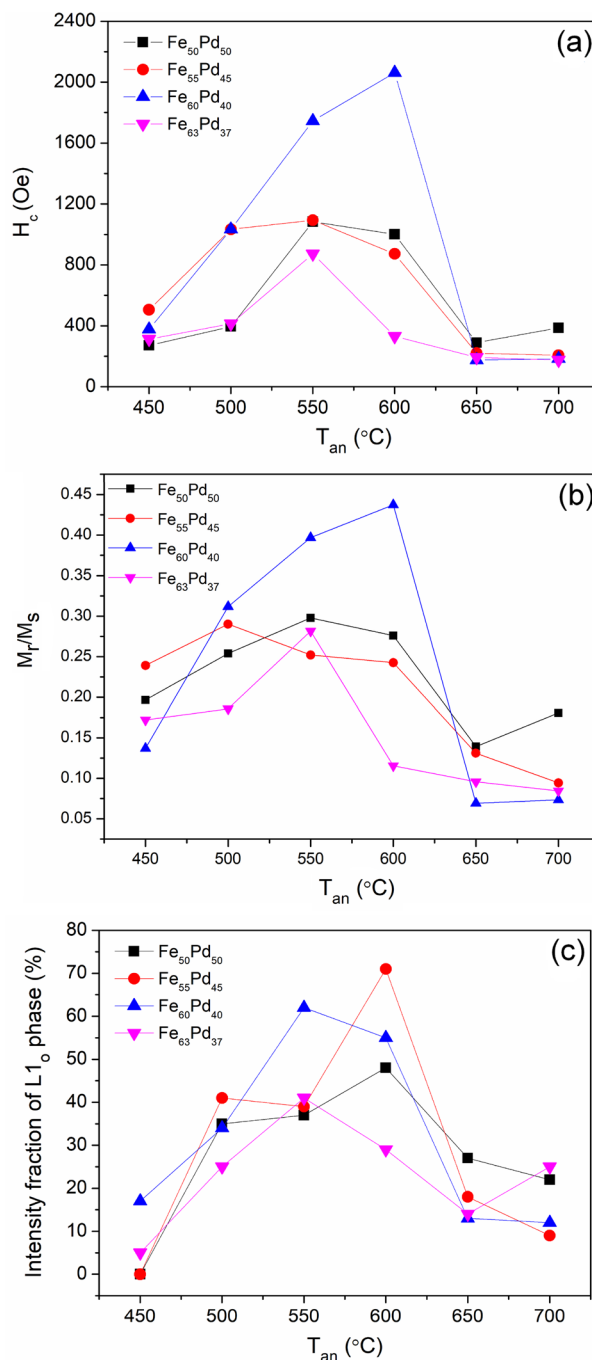
Fig. 6 Comparison of the low angle parts of the X-ray diffractograms taken on the $Fe_{50}Pd_{50}$ and $Fe_{55}Pd_{45}$ nanoparticles annealed at 700 °C
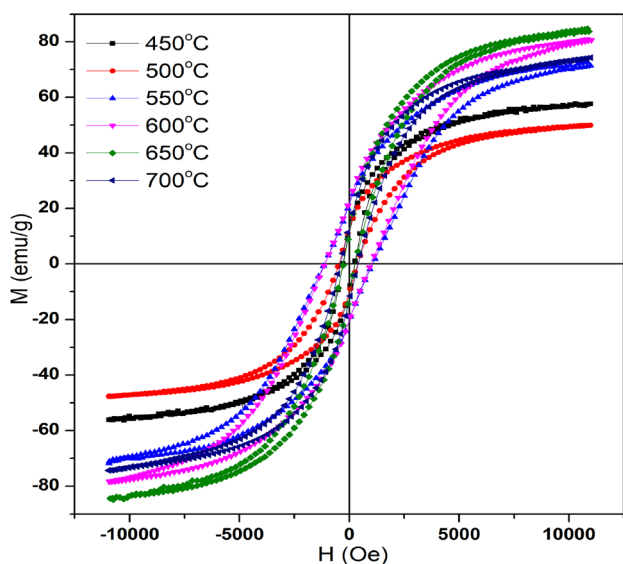
Fig. 7 Room-temperature magnetic hysteresis $M(H)$ loops of $Fe_{50}Pd_{50}$ nanoparticles annealed at different temperatures


Fig. 8 **a** Coercivity (H_C), **b** squareness ratio (M_r/M_S), and **c** intensity fraction of $L1_0$ phase versus annealing temperature for Fe_xPd_{100-x} ($x = 50, 55, 60$ and 63) nanoparticles measured at room temperature.

nanoparticles, which can avoid aggregation of nanoparticles caused by sintering. The authors obtained the optimum coercivity of 1.8 kOe but a rather low magnetization of 17 emu/g for the FePd nanoparticles of stoichiometry Fe:Pd = 1:1 [7, 33]. Our observed maximum value of H_C is also comparable to the values obtained for FePd thin films by Nguyen et al. [19] and Bahamida et al. [40]. Nguyen et al. [19] prepared off-stoichiometric FePd thin films deposited on MgO (001) substrates by magnetron sputtering. They reported the room-temperature perpendicular coercivity values of 0.39 kOe and 1.5 kOe in their films annealed at 700 °C for 1 and 10 h, respectively. Bahamida et al. [40] used the thermal evaporation to grow the $Fe_{56}Pd_{44}$ thin film on a silicon substrate

and annealed it at 550 °C for different times up to 2 h. They observed that the room-temperature coercivity increased with increasing annealing time, reaching a value of 157.1 kA/m (1.97 kOe) after annealing for 1 h. It is noted that in [26] no value of coercivity for the sample annealed for 2 h was reported.

It is worth noticing that when annealing CoPt and FePt thin films at 700 °C for up to 210 min and measuring the L1$_0$ ordered volume fraction (f_0) and the coercivity (H_C) as functions of anneal time using TEM and a SQUID magnetometer, respectively, Ristau et al. were able to establish a direct relationship between these two parameters [50]. They observed that H_C increased in proportion to f_0 until the sample was fully ordered. A similar trend was also observed by Toney et al. for FePt films [52], through a systematic study of the growth temperature dependence of f_0 and H_C. The origin of this dependence has been attributed to the strong dependence of the magnetocrystalline anisotropy on f_0 and its chemical order (s_0). Shih et al. reported that in addition to the $H_C(f_0)$ dependence, the remanent magnetization (M_r) to saturation magnetization (M_S), M_r/M_S, could also be used as a measure of chemical ordering degree of the L1$_0$ ordered phase (s_0) for FePt films [51]. To further understand the annealing temperature dependence of H_C for Fe$_x$Pd$_{100-x}$ nanoparticles (Fig. 8a), we have plotted M_r/M_S as a function of annealing temperature (T_{an}) and displayed the result in Fig. 8b. It is interesting to observe that M_r/M_S vs. T_{an} (Fig. 8b) follows a trend observed for the T_{an} dependence of H_C (Fig. 8a). The maximum values of H_C and M_r/M_S observed for T_{an} around 550–600 °C appear to correspond to the largest values of the volume fraction of the ordered FePd phase (L1$_0$ phase) achieved for those samples. This becomes clear when we assess in Fig. 8c the dependence of the volume fraction of the L1$_0$ phase on annealing temperature for Fe$_x$Pd$_{100-x}$ ($x=50$, 55, 60 and 63) nanoparticles.

To establish the correlation between the volume fraction of the ordered FePd phase and the coercivity of the samples investigated, we present in Fig. 9 a plot of the coercivity as a function of the L1$_0$ phase fraction (taken from Table 1) for these nanoparticles. It is very interesting to mention that the correlation between the coercivity and the L1$_0$ ordered phase fraction becomes nearly linear at high volume fractions of the L1$_0$ ordered phase, which is similar to that observed for FePt and CoPt thin films [50]. As can be seen from Fig. 9, the coercivity remained low even if the L1$_0$ phase fraction increased to 30%. It should be noted that the samples having L1$_0$ phase fraction lower than 30% are obtained in two ways. Some of them were annealed at low temperatures (450 °C for all samples and 500 °C for $x=50$ and 63). In these samples, there was no L1$_0$ phase, or its fraction was less than 35%. The other group of samples with low coercivity was obtained by annealing the nanoparticles at high temperatures (650 and 700 °C), and in these powders the L1$_0$ phase fraction was between 10 and 30%. The low coercivity can be caused by a reduced chemical order in this phase. The decrease of the chemical order in the L1$_0$ phase at high temperatures has also been observed in [36]. A specific case is the Fe$_{55}$Pd$_{45}$ sample annealed at 600 °C. From both Table 1 and Fig. 8, one can see that this sample
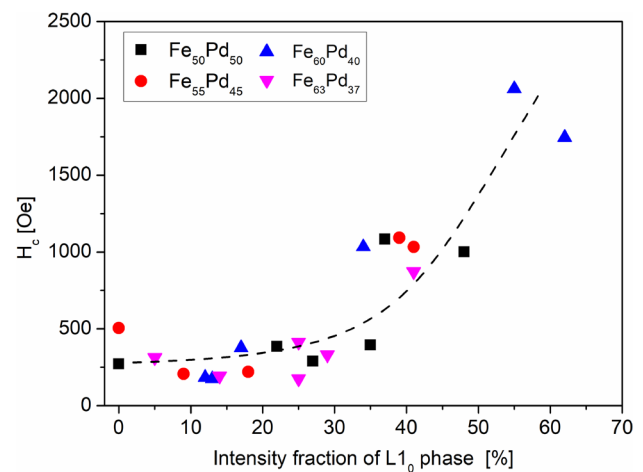
Fig. 9 Coercivity (H_C) as a function of intensity fraction of L1$_0$ phase for Fe$_x$Pd$_{100-x}$ nanoparticles

exhibits an abnormally large L1$_0$ ordered phase fraction as compared to the others while having a moderate value of H_C. The reduced chemical order in the L1$_0$ phase may cause the lower coercivity compared to that predicted from the trend line in Fig. 9. A former study on a Fe$_{52.3}$Pd$_{47.6}$ thin film revealed that with increasing deposition temperature from 400 to 500 °C, although the fraction of L1$_0$ phase slightly increased, the chemical order decreased simultaneously [36]. Due to the possible specific complexity of the structure in the Fe$_{55}$Pd$_{45}$ sample annealed at 600 °C, its point relating the coercivity and L1$_0$ ordered phase fraction is not incorporated in Fig. 9 for observing a general variation trend for all compositions. Finally, it is important to highlight that while previous studies failed to relate the magnetic coercivity to the L1$_0$ ordered FePd phase fraction in the Fe$_x$Pd$_{100-x}$ nanoparticle system due to the lack of a thorough analysis of phases created during synthesis or annealing, the combined TEM, STEM and magnetization data and analysis presented in this work have allowed us to establish, for the first time, this correlation, knowledge of which is the key to tailoring the hard magnetic properties of FePd-based and related nanomaterials for applications in energy-conversion and information technologies.

4 Conclusions

In summary, the Fe$_x$Pd$_{100-x}$ nanoparticles ($x=50$, 55, 60, and 63) were prepared by sonoelectrodeposition and characterized by the combination of magnetometry, XRD, STEM and EDS mapping. This synthesis method possesses some advantages (simple, efficient, low cost, and easy scale up) over other approaches [48, 63]. After annealing at temperatures between 450 and 700 °C, the nanoparticles exhibit hard

magnetic properties, which strongly depend on the chemical composition and the annealing temperature. The major phase in the as-prepared nanoparticles was a disordered fcc Pd(Fe) phase that transformed into a multi-phase material containing a $L1_0$ ordered FePd phase upon annealing. We found that with increasing annealing temperature, the volume fraction of $L1_0$ phase first increased, resulting in a considerable enhancement of coercivity. The maximum coercivity was achieved at temperature between 550 and 600 °C. For higher annealing temperatures, the volume fraction of $L1_0$ phase decreased, thus reducing the coercivity. Moreover, the reduction of the chemical order in this phase likely caused an additional magnetic softening. Based on these important findings, the correlation between the magnetic coercivity and the $L1_0$ ordered FePd phase fraction has been established for the Fe_xPd_{100-x} nanosystem.

Declarations

References

1. G.V.M. Williams, T. Prakash, J. Kennedy, S.V. Chong, S. Rubanov, J. Magn. Magn. Mater. **460**, 229 (2018)
2. J. Leveneur, J. Kennedy, G.V.M. Williams, J. Metson, A. Markwitz, Appl. Phys. Lett. **98**, 053111 (2011)
3. K.T. Arul, E. Manikandan, P.P. Murmu, J. Kennedy, M. Henini, J Alloys Compd. **720**, 395 (2017)
4. S. Ahmed, X. Ding, N. Bao, P. Bian, R. Zheng, Y. Wang, P.P. Murmu, J.V. Kennedy, R. Liu, H. Fan, K. Suzuki, J. Ding, J. Yi, Chem. Mater. **29**, 9066 (2017)
5. N.H. Nam, N.H. Luong, Nanoparticles: Synthesis and applications, in *Materials for Biomedical Engineering: Inorganic Micro and Nanostructures*. ed. by V. Grumezescu, A.M. Grumezescu (Elsevier, Amsterdam, 2019), p.211
6. D. Weller, A. Moser, L. Folks, M.E. Best, W. Lee, M.F. Toney, M. Schwickert, J.U. Thiele, M.F. Doerner, IEEE Trans. Magn. **36**, 10 (2000)
7. Z. Shao, S. Ren, Nanoscale Adv. **2**, 4341 (2020)
8. H. Lian, X. Cheng, H. Hao, J. Han, M.-T. Lau, Z. Li, Z. Zhou, Q. Dong, W.-Y. Wong, Chem. Soc. Rev. **51**, 1926 (2022)
9. B. Shen, S. Sun, Chem. Eur. J. **26**, 6757 (2020)
10. S. Sun, C.B. Murray, D. Weller, L. Folks, A. Moser, Science **287**, 1989 (2000)
11. D. Weller, G. Parker, O. Mosendz, A. Lyberatos, D. Mitin, N.Y. Safonova, M. Albrecht, J. Vac. Sci. Technol. B **34**, 060801 (2016)
12. B.D. Terris, T. Thomson, J. Phys. D: Appl. Phys. **38**, R199 (2005)
13. E. Mayes, A. Bewick, D. Gleeson, J. Hoinville, R. Jones, O. Kasyutich, A. Nartowski, B. Warne, J. Wiggins, K.K.W. Wong, IEEE Trans. Magn. **39**, 624 (2003)
14. N. Sakuma, T. Ohshima, T. Shoji, Y. Suzuki, R. Sato, A. Wachi, A. Kato, Y. Kawai, A. Manabe, T. Teranishi, ACS Nano **5**, 2806 (2011)
15. T. Klemmer, D. Hoydick, H. Okumura, B. Zhang, W.A. Soffa, Scr. Metall. Mater. **33**, 1793 (1995)
16. D.H. Wei, Y.D. Yao, Appl. Phys. Lett. **95**, 172503 (2009)
17. P. Tiberto, G. Barrera, F. Celegato, M. Coisson, E.S. Olivetti, F. Vinai, J. Alloy Compd. **615**(Supplement 1), S236 (2014)
18. C.H. Hsiao, Y.D. Yao, S.C. Lo, H.W. Chang, H. Ouyang, Appl. Phys. Lett. **107**, 142407 (2015)
19. D.C. Nguyen, C.C. Chu, C.H. Lee, W.C. Lai, C.S. Chang, J. Appl. Phys. **123**, 073901 (2018)
20. K. Sato, B. Bian, Y. Hirotsu, J. Appl. Phys. **91**, 8516 (2002)
21. K. Sato, Y. Hirotsu, J. Appl. Phys. **93**, 6291 (2003)
22. K. Sato, T.J. Konno, Y. Hirotsu, J. Appl. Phys. **105**, 034308 (2009)
23. K. Sato, K. Aoyagi, T.J. Konno, J. Appl. Phys. **107**, 024304 (2010)
24. Y. Hou, H. Kondoh, T. Kogure, T. Ohta, Chem. Mater. **16**, 5149 (2004)
25. Y. Hou, H. Kondoh, T. Ohta, J. Nanosci. Nanotechnol. **9**, 202 (2009)
26. M. Chen, D.E. Nikles, J. Appl. Phys. **91**, 8477 (2002)
27. S. Kang, Z. Jia, D.E. Nikles, J.W. Harrell, J. Appl. Phys. **95**, 6744 (2004)
28. K. Watanabe, H. Kura, T. Sato, Sci. Tech. Adv. Mater. **7**, 145 (2006)
29. N.S. Gajbhiye, S. Sharma, R.S. Ningthoujam, J. Appl. Phys. **104**, 123906 (2008)
30. S. Sharma, N.S. Gajbhiye, R.S. Ningthoujam, A.I.P. Conf, Proc. **1313**, 125 (2010)
31. H.L. Nguyen, L.E.M. Howard, S.R. Giblin, B.K. Tanner, I. Terry, A.K. Hughes, I.M. Ross, A. Serres, H. Burckstummer, J.S.O. Evans, J. Mater. Chem. **15**, 5136 (2005)
32. Z. Meng, G. Li, N. Zhu, C.-L. Ho, C.-W. Leung, W.-Y. Wong, J. Organomet. Chem. **849–850**, 10 (2017)
33. Z. Shao, L. An, Z. Li, Y. Huang, Y. Hu, S. Ren, Chem. Commun. **56**, 6555 (2020)
34. H. Xu, H. Heinrich, J.M.K. Wiezorek, Intermetallics **11**, 963 (2003)
35. Ch. Issro, W. Puschl, W. Pfeiler, P.F. Rogl, W.A. Soffa, M. Acosta, G. Schmerber, R. Kozubski, V. Pierron-Bohnes, Scr. Mater. **53**, 447 (2005)
36. C. Clavero, J.M. Garcia-Martin, J.L. Costa Kramer, G. Armelles, A. Cebollada, Y. Huttel, R.A. Lukaszew, A.J. Kellock, Phys. Rev. B **73**, 174405 (2006)

37. M. Cialone, F. Celegato, M. Coisson, G. Barrera, G. Fiore, R. Shvab, U. Klement, P. Rizzi, P. Tiberto, Sci. Rep. **7**, 16691 (2017)
38. S.N. Hsiao, C.C. Chen, S.H. Liu, S.K. Chen, Vacuum **187**, 110153 (2021)
39. M.N. Shamis, N.Y. Schmidt, T.I. Verbytska, P.V. Makushko, G. Beddies, M. Albrecht, Yu.N. Makogon, Appl. Nanosci. **12**, 1227 (2022)
40. S. Bahamida, A. Fnidiki, M. Coisson, G. Barrera, F. Celegato, E.S. Olivetti, P. Tiberto, A. Laggoun, M. Boudissa, Thin Solid Films **668**, 9 (2018)
41. H.A. Durr, E. Dudzik, S.S. Dhesi, J.B. Goedkoop, G. van der Laan, M. Belakhovsky, C. Mocuta, A. Marty, Y. Samson, Science **284**, 2166 (1999)
42. F.M. Takata, G. Pattanaik, W.A. Soffa, P.T.A. Sumodjo, G. Zangari, Electrochem. Commun. **10**, 568 (2008)
43. H.P. Lin, J.C. Kuo, Mater. Lett. **65**, 3537 (2011)
44. G. Barrera, F. Scaglione, M. Cialone, F. Celegato, M. Coisson, P. Rizzi, P. Tiberto, Materials **13**, 1454 (2020)
45. N.T.T. Van, T.T. Trung, N.H. Nam, N.D. Phu, N.H. Hai, N.H. Luong, Eur. Phys. J. Appl. Phys. **64**, 10403 (2013)
46. N.H. Luong, T.T. Trung, T.P. Loan, L.M. Kien, T.T. Hong, N.H. Nam, J. Electron. Mater. **45**, 4309 (2016)
47. N.H. Luong, T.T. Trung, T.P. Loan, N.H. Nam, P. Jenei, J.L. Labar, J. Gubicza, J. Electron. Mater. **46**, 3720 (2017)
48. J. Zhu, S.T. Aruna, Y. Koltypin, A. Gedanken, Chem. Mater. **12**, 143 (2000)
49. T.J. Mason, J.P. Lorimer, D.J. Walton, Ultrasonics **28**, 333 (1990)
50. R.A. Ristau, K. Barmak, L.H. Lewis, K.R. Coffey, J.K. Howard, J. Appl. Phys. **86**, 4527 (1999)
51. J.-C. Shih, H.-H. Hsiao, J.-L. Tsai, T.-S. Chin, IEEE Trans. Magn. **37**, 1280 (2001)
52. M.F. Toney, W.-Y. Lee, J.A. Hedstrom, A. Kellock, J. Appl. Phys. **93**, 9902 (2003)
53. J. Gubicza, *X-ray line profile analysis in Materials Science* (IGI-Global, Hershey, PA, USA, 2014)
54. Y.M. Mos, A.C. Vermeulen, C.J.N. Buisman, J. Weijma, Geomicrobiol. J. **35**, 511 (2018)
55. https://www.azom.com/article.aspx?ArticleID=20003
56. N.I. Vlasova, A.G. Popov, N.N. Shchegoleva, V.S. Gaviko, L.A. Stashkova, G.S. Kandaurova, D.V. Gunderov, Acta Mater. **61**, 2560 (2013)
57. K.S. Suslick, S.B. Choe, A.A. Cichowlas, M.W. Grinstaff, Nature **353**, 414 (1991)
58. A. Gedanken, Ultrason. Sonochem. **11**, 47 (2004)
59. K.S. Suslick, *Ultrasound: its chemical, physical and biological effects* (VCH, New York, 1988)
60. Yu. Koltypin, X. Cao, R. Prozorov, J. Balogh, D. Kaptas, A. Gedanken, J. Mater. Chem. **7**, 2453 (1997)
61. T. Prozorov, R. Prozorov, A. Snezhko, K.S. Suslick, Appl. Phys. Let. **83**, 2019 (2003)
62. N.H. Luong, N.H. Hai, N.D. Phu, D.A. MacLaren, Nanotechnology **22**, 285603 (2011)
63. N.H. Nam, N.T.T. Van, N.D. Phu, T.T. Hong, N.H. Hai, N.H. Luong, J. Nanomater. **2012**, 801240 (2012)